Thermal Emission Imaging System (THEMIS) infrared observations of atmospheric dust and water ice cloud optical depth

Michael D. Smith

NASA Goddard Space Flight Center, Greenbelt, Maryland, USA

Joshua L. Bandfield and Philip R. Christensen

Department of Geology, Arizona State University, Tempe, Arizona, USA

Mark I. Richardson

Division of Geological and Planetary Sciences, California Institute of Technology, Pasadena, California, USA

[1] The Mars Odyssey spacecraft entered into Martian orbit in October 2001 and after successful aerobraking, began mapping in February 2002. Thermal infrared images taken by the Thermal Emission Imaging System (THEMIS) on board the Odyssey spacecraft allow for the quantitative retrieval of atmospheric dust and water ice aerosol optical depth. Data collected so far cover late northern winter, spring, and summer ($L_s = 330°-160°$). During this period, THEMIS observed the decay of a regional dust storm, a number of local dust storms along the edge of the retreating north polar cap, and the growth of the low-latitude aphelion water ice cloud belt. Data from THEMIS complements the concurrent Mars Global Surveyor Thermal Emission Spectrometer (TES) data by sampling a later local time (~1400 LT for TES versus ~1600–1730 LT for THEMIS) and by observing at much higher spatial resolution. Comparison of water ice optical depth in the aphelion cloud belt from THEMIS and TES shows a significantly higher optical depth in the late afternoon (THEMIS) than in the early afternoon (TES).   *INDEX TERMS:* 6225 Planetology: Solar System Objects: Mars; 5409 Planetology: Solid Surface Planets: Atmospheres—structure and dynamics; 5464 Planetology: Solid Surface Planets: Remote sensing; 3360 Meteorology and Atmospheric Dynamics: Remote sensing; 0305 Atmospheric Composition and Structure: Aerosols and particles (0345, 4801); *KEYWORDS:* Mars, THEMIS, dust, water ice, optical depth, cloud

Citation: Smith, M. D., J. L. Bandfield, P. R. Christensen, and M. I. Richardson, Thermal Emission Imaging System (THEMIS) infrared observations of atmospheric dust and water ice cloud optical depth, *J. Geophys. Res.*, *108*(E11), 5115, doi:10.1029/2003JE002115, 2003.

1. Introduction

[2] The Thermal Emission Imaging System (THEMIS) on board the Mars Odyssey spacecraft contains both visible/near-IR (450–850 nm) and thermal infrared (6.5–15 μm) channels. The infrared observations, which are the topic of this report, build upon a long history of observations from similar thermal infrared instruments at Mars, including the Mariner 9 Infrared Interferometer Spectrometer (IRIS) [*Hanel et al.*, 1972], the Viking Infrared Thermal Mapper (IRTM) [*Chase et al.*, 1978; *Kieffer et al.*, 1977], and the Mars Global Surveyor Thermal Emission Spectrometer (TES) [*Christensen et al.*, 1992, 2001].

[3] Although the primary goals of the THEMIS instrument are to determine surface mineralogy and to study small-scale geologic processes and thermophysical proper-ties, atmospheric science is also a priority of the THEMIS science team. The spectral range covered by THEMIS contains strong signatures of atmospheric dust and water ice aerosols and is well suited for the quantitative retrieval of aerosol optical depth.

[4] Previous spacecraft missions have already made a significant contribution to our understanding of the present Martian climate. The Martian atmosphere exhibits very striking and generally repeatable annual patterns [e.g., *Clancy et al.*, 2000; *Smith et al.*, 2001a, 2001b; *Liu et al.*, 2003] in temperature, aerosol loading, and water vapor column. There are two distinct seasons on Mars. The perihelion season (roughly northern fall and winter) is characterized by relatively warm and dusty conditions. In contrast, the aphelion season (roughly northern spring and summer) is relatively cool, free of dust, and cloudy [*Clancy et al.*, 1996, 2000; *Smith et al.*, 2001a, 2001b]. The observations presented here cover the aphelion season of 2002–2003. Although one moderate regional dust storm

was observed at the beginning of the Odyssey mapping, the main atmospheric event during this period was the initiation and growth of the low-latitude belt of water ice clouds that circles the globe during the aphelion season [*Clancy et al.*, 1996; *Pearl et al.*, 2001].

[5] Dust and water ice optical depth retrieved from THEMIS is complementary to the same values retrieved from concurrent TES observations by sampling a later local time (~1400 LT for TES versus ~1600–1730 LT for THEMIS). Comparison of aerosol optical depth from simultaneous TES and THEMIS observations allows for a limited investigation of the diurnal cycle of dust and water ice. The continued monitoring of aerosol optical depth by THEMIS also serves to maintain the near-continuous record begun by TES in the event of a failure by the aging Mars Global Surveyor spacecraft or TES instrument. Finally, the successful interpretation of THEMIS data for mineralogical identification requires an accurate correction to account for atmospheric contribution. Results from TES have underscored the importance of properly separating the atmospheric and surface contributions to the observed spectrum for quantitative analysis [*Smith et al.*, 2000b; *Bandfield et al.*, 2000a; *Christensen et al.*, 2000] and the care that must be taken to perform that separation properly. The observed strong spatial and temporal variations of aerosol optical depth make characterization of those quantities from the THEMIS data itself crucial for proper atmospheric correction. Therefore the retrieval of atmospheric aerosol optical depth using THEMIS infrared data is also a critical part of the successful completion of THEMIS surface science objectives.

2. Data Set

2.1. THEMIS Instrument

[6] The THEMIS instrument contains a thermal infrared wavelength focal plane with 10 spectral filters ranging from 6.5 to 15 μm, and a visible wavelength focal plane with five spectral filters ranging from 450 to 850 nm [*Christensen et al.*, 2003a, 2003b]. Although atmospheric observations using the visible light filters can be used to identify water ice and dust clouds, we concern ourselves here with data from the thermal infrared only.

[7] THEMIS infrared images are 320 pixels wide with a spatial resolution of 100 m/pixel, so the images are 32 km wide. Images are of variable length, often stretching for several thousand pixels along the orbit track (which runs in a roughly north-south direction). At each pixel, infrared data is returned in up to 10 spectral bands. THEMIS bands 1 and 2 have the same spectral response, so there are nine distinct spectral bands with centers at 6.78, 7.93, 8.56, 9.35, 10.21, 11.04, 11.79, 12.57, and 14.88 μm, respectively for bands 1 or 2 through 10. Each spectral band has a bandwidth of about 1.0 μm. Figure 1 shows the spectral response of the THEMIS bands.

[8] The data have been calibrated to spectral radiance (W cm^{-2} ster^{-1} μm^{-1}) to remove the instrument response function and stray light reflections. THEMIS has a single-pixel noise equivalent spectral radiance (NESR) of 2.72 × 10^{-6} W cm^{-2} ster^{-1} μm^{-1} in band 9, corresponding to a 1σ noise equivalent delta temperature of 0.4 K at 245 K (typical daytime temperature).
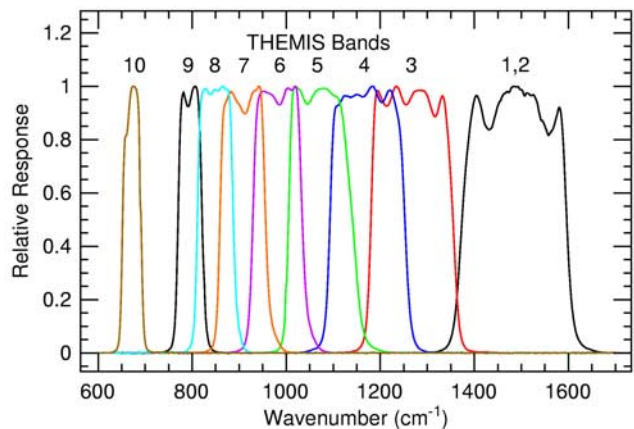

Figure 1. The spectral response of the 10 THEMIS bands. Note that THEMIS bands 1 and 2 have the same spectral response.

[9] Although the retrieval of aerosol optical depth takes only a small fraction of a second, it is still not practical to perform on a pixel-by-pixel basis for a large number of images because of the large number of pixels in THEMIS infrared images. Instead, we perform the retrieval on blocks of data called "framelets," which are spatial resolution elements 320 pixels wide (the width of the image) by 256 pixels long (along track). Each framelet is thus 32 × 26 km, or roughly one third of a degree square. This spatial resolution is sufficient to resolve most atmospheric variations of interest, and the capability for spatial averaging of any size (including pixel by pixel) has been retained for special investigations involving small-scale processes. Because a THEMIS image has arbitrary length, there can be anywhere from one to several dozen framelets in a single image.

2.2. THEMIS Observation Strategy

[10] Because of its high spatial resolution and wide cross-track field of view, THEMIS collects over 200 times as much data per unit distance along the orbit track as does TES. Therefore, even at the highest data rates, THEMIS cannot return to Earth continuous pole-to-pole coverage as TES can. Instead, data volume has been divided between targeting specific locations of scientific interest based on THEMIS Science Team input and a systematic mapping of the entire planet. In general, there are enough geologically interesting regions throughout the globe that reasonably good global spatial coverage is achieved on average over a time period of 5° of L_s. In addition, approximately every 5° of L_s, a special sequence has been run for atmospheric science to take a set of small images in a latitude-longitude grid in at attempt to fill in any gaps (in latitude and longitude coverage) that might be left by the imaging of geologic targets.

[11] Whenever 10 band infrared images are taken, as long as there is sufficient thermal contrast between the surface and atmosphere, atmospheric properties can be retrieved regardless of the primary purpose for taking the image at a certain location. A total of 67,374 framelets from over 4000 along-track image strips were used in this study. Images were taken between 19 February 2002 (L_s = 330°) and
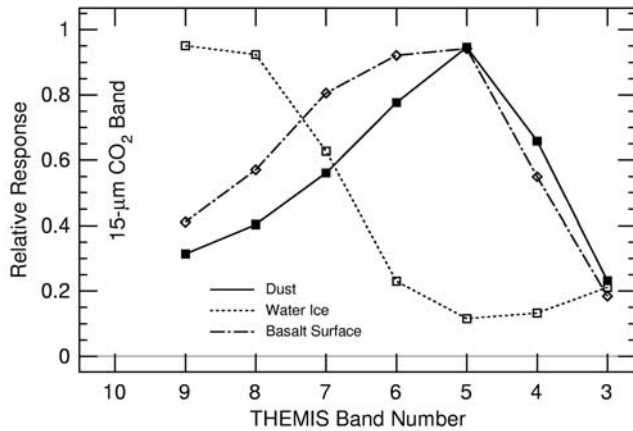
Figure 2. The spectral dependence of absorption features caused by dust (solid line and solid boxes), water ice (dotted line and open boxes), and a basaltic nonunit surface emissivity (dash-dotted line and diamonds) at THEMIS spectral resolution.

31 March 2003 ($L_s = 161°$). The framelets are distributed nearly uniformly over the period of data acquisition and there are no gaps in the coverage longer than 5° of L_s. Within this period, the local time for the observations increases almost linearly from 1500 LT at $L_s = 330°$ to 1710 LT at $L_s = 161°$.

3. Retrieval Algorithm

[12] The THEMIS infrared images allow for the quantitative retrieval of atmospheric dust and water ice aerosol optical depth. Following the algorithms used for TES [*Smith et al.*, 2000a], dust and water ice optical depth are retrieved simultaneously in a separate step after the atmospheric temperature profile $T(p)$ has been estimated. The basic idea is to find the values of dust and water ice optical depth that provide the best fit between computed and observed radiance. The observations we use are THEMIS bands 3–8. Bands 1 and 2 are not used because of contributions from water vapor and surface emissivity effects, and because of uncertainties in the aerosol spectral dependence in that spectral region. Band 9 is not used because of contributions from the wings of the 15 μm CO_2 band.

[13] If we neglect the small contributions from the solar beam and scattering from atmospheric aerosols (section 3.4), and assume a plane-parallel atmosphere, the observed monochromatic radiance of Mars as a function of wave number, $I_{obs}(\nu)$, can be written as

$$I_{obs}(\nu) = \epsilon(\nu) \, B[T_{surf}, \nu] \, e^{-\tau_0(\nu)/\mu} + \int_0^{\tau_0(\nu)} B[T(\tau), \nu] \, e^{-\tau/\mu} d\tau,$$

(1)

where $\epsilon(\nu)$ is the surface emissivity at frequency ν, $\tau_0(\nu)$ is the normal column-integrated aerosol optical depth, μ is the cosine of the emission angle, $B[T, \nu]$ is the Planck function, T_{surf} is the surface temperature, $T(\tau)$ is the atmospheric temperature, and the integral is performed from the spacecraft (at $\tau = 0$) to the surface (at $\tau = \tau_0$).

[14] As described below, we estimate surface emissivity, ϵ, and atmospheric temperature, $T(p)$, from TES data, the

emission angle, μ, is known, and we solve for the dust and water ice aerosol contributions to optical depth τ_0. The surface temperature is initially estimated from the THEMIS data and is corrected in a self-consistent way as τ_0 is varied (see below).

3.1. Atmospheric Temperature

[15] THEMIS spectra do not have the spectral resolution necessary to retrieve an atmospheric temperature profile from the 15 μm CO_2 band. The one THEMIS band (# 10) in the CO_2 absorption band was designed to give a temperature that is representative of a broad region of the atmosphere (roughly 0.1–2.0 mbar), analogous to the "T15" temperature derived from the Viking IRTM instrument [*Martin and Kieffer*, 1979]. However, calibration of THEMIS band 10 data has failed to give temperatures that are accurate enough to be useful for estimation of atmospheric temperatures. Therefore we estimate atmospheric temperature as a function of pressure, $T(p)$, using concurrent TES data at the same latitude [*Conrath et al.*, 2000]. While there is a difference in local time between TES (~1400 LT) and THEMIS (1600–1730 LT) observations, GCM results [*Wilson and Richardson*, 2000] show that the expected temperature difference between 1400 LT and 1700 LT is usually no greater than other uncertainties (a few K), so no local time extrapolation of atmospheric temperatures was attempted.

3.2. Spectral Dependence of Aerosols and Surface Emissivity

[16] The total aerosol optical depth τ_0 is computed by adding the contributions from dust and water ice:

$$\tau_0(\nu) = A_{dust} f_{dust}(\nu) + A_{ice} f_{ice}(\nu),$$

(2)

where f_{dust} and f_{ice} describe the spectral dependence of dust and water ice optical depth, and A_{dust} and A_{ice} are scaling factors that give the optical depth of dust and ice at standard frequencies where the functions f are defined to be unity. We define $f_{dust} \equiv 1$ at 1075 cm^{-1} and $f_{ice} \equiv 1$ at 825 cm^{-1} to correspond to the peak absorption of the two aerosols.

[17] Figure 2 shows the spectral dependence of absorption features caused by dust, water ice, and a nonunit surface emissivity basaltic surface at THEMIS spectral resolution. Numerical values for each THEMIS band used in the retrieval are given in Table 1. These functions have been derived from TES nadir and emission phase function (EPF) data [*Smith et al.*, 2000b; *Bandfield et al.*, 2000a; *Bandfield and Smith*, 2003]. Notice that the dust and water ice spectral features are resolved and well described even at the relatively low spectral resolution of THEMIS. However, notice also that the spectral dependence of dust and the

Table 1. Spectral Dependence of Dust (f_{dust}), Water Ice (f_{ice}), and Basalt Surface (f_{surf}) Convolved to THEMIS Spectral Resolution

Band	Dust	Water Ice	Surface
3	0.23	0.21	0.18
4	0.66	0.13	0.55
5	0.95	0.12	0.94
6	0.78	0.23	0.92
7	0.56	0.63	0.81
8	0.40	0.92	0.57
9	0.31	0.95	0.41

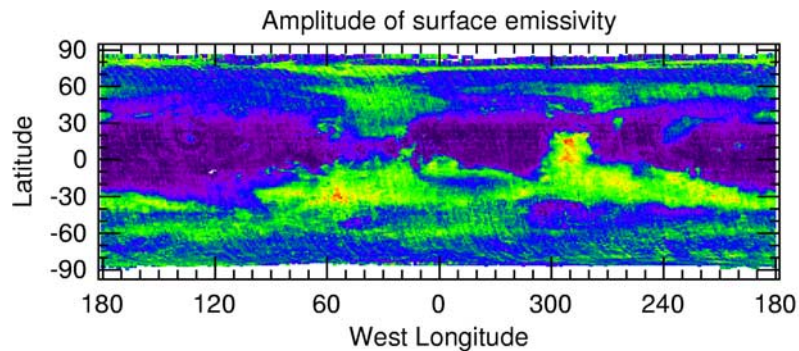Amplitude of surface emissivity

Figure 3. Map of the amplitude of the basaltic surface emissivity feature, A_{surf}, as derived from TES data. The color scale goes from 0 (purple) to 0.075 (red). Surface emissivity is given as $(1 - A_{surf} f_{surf})$, where f_{surf} is the spectral shape of surface emissivity shown in Figure 2 (dash-dotted line).

basaltic surface are very similar over this spectral range. This makes it difficult to separate their contributions using THEMIS data alone. Observations by TES can separate the relative contributions of dust and the surface because the spectral dependence of the two are quite different at the longer wavelengths (20–50 μm) that can be observed by TES [*Smith et al.*, 2000b]. Therefore we have chosen to model surface emissivity using a map derived from TES data and shown in Figure 3. Surface emissivity, $\epsilon(\nu)$ is given by

$$\epsilon(\nu) = (1 - A_{surf} f_{surf}(\nu)), \qquad (3)$$

where A_{surf} is the amplitude of the basaltic surface emissivity feature.

[18] The three spectral shapes above for dust, water ice, and surface emissivity are used for all THEMIS spectra. Although recent emission phase function observations [*Clancy et al.*, 2003] show that aerosol particle properties depend somewhat on location and season, our experience with TES data is that the spectral dependence of dust and water ice optical depth at thermal infrared wavelengths does not change by an amount great enough to significantly change the retrieved amplitudes of dust and water ice (A_{dust} and A_{ice}) [*Smith et al.*, 2000a, 2000b; *Bandfield et al.*, 2000a; *Bandfield and Smith*, 2003].

3.3. Surface Temperature

[19] THEMIS band 3 is used to make an initial estimate for surface temperature because in that spectral region the atmosphere is the most transparent and the surface emissivity of most rock-forming minerals is near unity. However, the spectral bandpass of band 3 is fairly wide and contains a noticeable optical depth from dust and water ice, hence it includes a nonunit surface emissivity contribution. We account for this by adjusting the surface temperature in a self-consistent way according to the given surface emissivity and the retrieved optical depth of dust and water ice.

3.4. Simplifying Approximations

[20] In a similar way as was done with the TES aerosol retrievals [*Smith et al.*, 2000a], three main approximations are made to simplify the retrieval process. The first approximation is that dust is assumed to be well mixed with the background gas. Although not strictly true, experience with Viking [*Pollack et al.*, 1977; *Jaquin et al.*, 1986], Pathfinder

[*Smith et al.*, 1997], and our own experience with TES is that for dust the well-mixed approximation is usually very good, and we expect that this approximation is not a major source of uncertainty. Note however, that the water ice aerosol is not assumed to be well mixed. We assume that water ice aerosols are in the form of condensate clouds, so that there is no water ice aerosol below the water condensation level. We compute the water condensation level using an atmospheric temperature profile and water vapor column abundance retrieved from concurrent TES observations. The water ice aerosol is assumed to be well mixed above the condensation level. Knowledge of the vertical distribution of the aerosol allows the atmospheric temperature $T(\tau)$ in equation (1) to be replaced by with $T(p)$, which is the quantity that is directly retrieved from the 15 μm CO_2 band [*Conrath et al.*, 2000].

[21] The second approximation is to neglect scattering caused by dust and ice aerosols. By neglecting scattering the value we retrieve here is the effective absorption optical depth, not the full extinction optical depth. We have performed numerical experiments where the retrieval algorithm for absorption optical depth used here was run on synthetic spectra computed including scattering. The results show that the retrieved absorption optical depth is almost linear in the actual extinction optical depth. For low and moderate optical depth (<0.5), extinction optical depth is about 1.3 times absorption optical depth for dust and about 1.5 times absorption optical depth for water ice aerosol. For higher optical depth (>0.5), the ratio between extinction and absorption optical depth becomes gradually larger. The exact value of the ratio between extinction and absorption optical depth depends on the aerosol size, shape, composition, and it is not a constant function of wave number. However, for all reasonable sizes and shapes of dust and water ice aerosols, the ratios at the wave number of peak absorption (825 cm^{-1} for water ice and 1075 cm^{-1} for dust) will be similar to the values given above. For example, *Wolff and Clancy* [2003] derive ratios of 1.3 and 1.4 for dust and water ice, respectively.

[22] The third approximation is that a single set of three spectral shapes (optical depth as a function of frequency) for dust, water ice, and surface emissivity can be used to fit all spectra. Although *Clancy et al.* [2003] and *Wolff and Clancy* [2003] report on differences in aerosol particle sizes for both dust and water ice, our own numerical experiments

show that variation of the aerosol spectral shapes to account for the particle size and shape changes leads to a change in the retrieved optical depth of ~ 0.01 or less. Likewise, changing the surface emissivity spectral shape from the "Type 1" to "Type 2" surfaces of *Bandfield et al.* [2000b] leads to a change in retrieved aerosol optical depth of a similar amount.

3.5. Retrieval Solution

[23] We use the starting assumption that within THEMIS band 3 the aerosol optical depth is zero ($\tau_0 = 0$). In that case, equations (1) and (3) simplify to

$$I_{obs}(\nu) = (1 - A_{surf} f_{surf}(\nu)) \, B[T_{surf}, \nu], \qquad (4)$$

and we can numerically solve for T_{surf} using the observed band 3 radiance, the assumed surface emissivity spectral dependence f_{surf} (Figure 2), the surface emissivity amplitude, A_{surf}, via a map derived from TES analysis (Figure 3), and the known spectral response of THEMIS band 3.

[24] The best fit for aerosol optical depth to observed THEMIS bands 3–8 is accomplished by iterative linear least squares. The initial iteration begins with $A_{dust} = A_{ice} = 0$. At the beginning of each iteration, the computed radiance, J_i, for each THEMIS band i is linearized about the current guess for optical depth in that band:

$$J_i = J_i(\tau_i) + \Delta\tau_i \frac{dJ_i}{d\tau} + \Delta T_{surf} \frac{dJ_i}{dT_{surf}}, \qquad (5)$$

where the optical depth increment $\Delta\tau_i$ is

$$\Delta\tau_i = \Delta A_{dust} f_{dust}(i) + \Delta A_{ice} f_{ice}(i) \qquad (6)$$

and the surface temperature increment is adjusted in a self-consistent way according to the optical depth increment using

$$\Delta T_{surf} = \Delta\tau_3 \frac{dT_{surf}}{d\tau_3}. \qquad (7)$$

The derivative in equation (7) is computed numerically using

$$\frac{dT_{surf}}{d\tau_3} = \left(\frac{dJ_3}{d\tau_3}\right) \Big/ \left(\frac{dJ_3}{dT_{surf}}\right). \qquad (8)$$

[25] Now, let

$$X_i = \frac{dJ_i}{dA_{dust}} + \frac{dJ_i}{dT_{surf}} \frac{dT_{surf}}{dA_{dust}} \qquad (9)$$

$$Y_i = \frac{dJ_i}{dA_{ice}} + \frac{dJ_i}{dT_{surf}} \frac{dT_{surf}}{dA_{ice}}; \qquad (10)$$

then, equation (5) becomes

$$J_i = J_i(\tau_i) + X_i \Delta A_{dust} f_{dust}(i) + Y_i \Delta A_{ice} f_{ice}(i). \qquad (11)$$

[26] The least squares solution is then found by the minimization of $Q = \sum_{i=3}^{i=8} (J_i - I_i)^2$ with respect to A_{dust}

and A_{ice}, where I_i is the observed radiance in THEMIS band i. This gives the matrix equation

$$\begin{bmatrix} \sum X_i^2 & \sum X_i Y_i \\ \sum X_i Y_i & \sum Y_i^2 \end{bmatrix} \begin{bmatrix} \Delta A_{dust} \\ \Delta A_{ice} \end{bmatrix} = \begin{bmatrix} \sum X_i(J_i - I_i) \\ \sum Y_i(J_i - I_i) \end{bmatrix}, \qquad (12)$$

where all sums are over THEMIS bands 3–8. The 2×2 matrix is easily inverted to solve for the increments in dust optical depth, ΔA_{dust}, and water ice optical depth, ΔA_{ice}. The iteration is completed by adding the ΔA values to A_{dust} and A_{ice} and then adjusting the surface temperature using equations (6) and (7).

[27] Nonlinearity in the equation of radiative transfer is accounted for by performing additional iterations until the solution converges ($\Delta A \rightarrow 0$). Typically convergence is rapid, requiring three or fewer iterations.

3.6. Estimation of Uncertainties

[28] Uncertainty in the retrieved values of dust and water ice optical depth come from a number of sources including instrument noise and calibration, error in the assumed temperature profile and surface emissivity, and simplifying assumptions of fixed spectral shapes and a well-mixed nonscattering aerosol. The formal propagation of random instrument noise leads to negligible error since we average over 320×256 pixel framelets. Uncertainty from calibration and other systematic errors is larger since they are not reduced by averaging pixels. We estimate the combined uncertainty from direct inputs into the retrieval (instrument radiance error, atmospheric temperature profile, and surface emissivity) to be roughly 0.02 or 10% of the total optical depth, whichever is larger.

[29] We have performed numerical experiments to evaluate the error introduced by the assumption of fixed spectral shapes. We used a suite of different aerosol and surface emissivity spectral shapes to compute synthetic spectra, and then retrieved aerosol optical depth using our fixed set of spectral shapes. In all cases the errors in both dust and water ice optical depth were 0.02 or less. The error caused by dust not being well mixed (as it is assumed to be) is likely <0.01 based on our experience with TES data, and we estimate that the error caused by our formulation of the vertical distribution of water ice is <0.02.

[30] Adding all uncertainties together we estimate the total uncertainty for any single framelet retrieved absorption optical depth is roughly 0.04 or 10% of the total absorption optical depth, whichever is larger. This estimate for the uncertainty in optical depth does not include the systematic difference between absorption and extinction optical depth. As stated earlier, we estimate that the extinction optical depth (including scattering) is systematically higher than the absorption optical depth by $\sim 30\%$ for dust and $\sim 50\%$ for water ice.

4. Results

[31] The results presented below were derived using data from the first one half Martian year of Mars Odyssey mapping, or $L_s = 330°$ (19 February 2002) to $L_s = 161°$ (31 March 2003). In Figures 4 and 5 we show the seasonal and spatial variation of dust and water ice aerosol optical
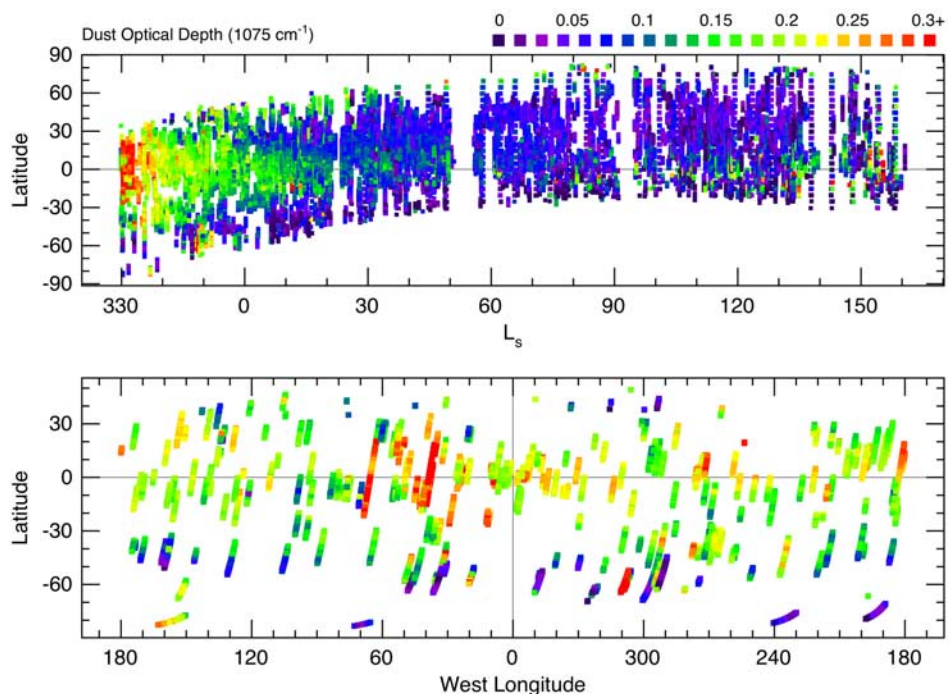
Figure 4. Dust optical depth (1075 cm^{-1}) scaled to an equivalent 6.1 mbar surface, as retrieved from daytime THEMIS infrared spectra. (top) An overview of THEMIS dust optical depth retrievals shown as a function of season (L_s) and latitude. Each individual point shows the retrieval from an individual framelet. The systematic grids (for example, $L_s = 138°$ and 143°) come from dedicated atmospheric observations. (bottom) Map of THEMIS dust optical depth for the period $L_s = 330°-350°$, showing the spatial structure of a decaying large regional dust storm. The color scale goes from 0 (purple) to 0.3 (red).
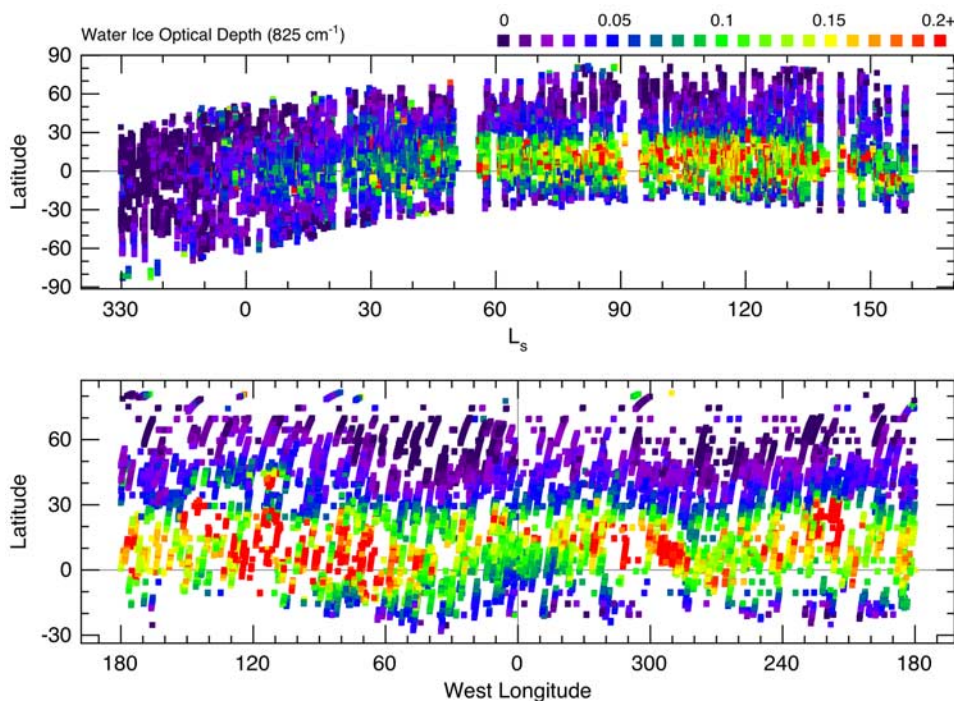

Figure 5. Water ice optical depth (825 cm^{-1}) as retrieved from daytime THEMIS infrared spectra. (top) An overview of THEMIS water ice optical depth retrievals shown as a function of season (L_s) and latitude. Each individual point shows the retrieval from an individual framelet. The systematic grids (for example, $L_s = 138°$ and 143°) come from dedicated atmospheric observations. (bottom) Map of THEMIS water ice optical depth for the period $L_s = 60°-120°$, showing the spatial structure of the aphelion season cloud belt. The color scale goes from 0 (purple) to 0.2 (red).
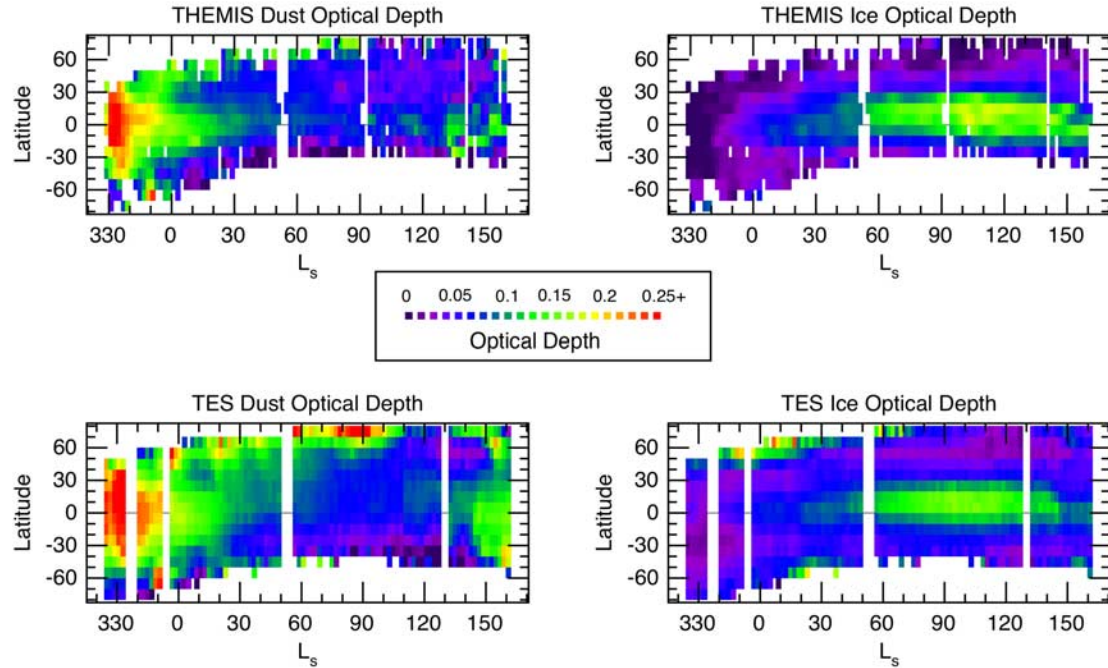
Figure 6. Comparison of concurrent aerosol optical depth retrievals using THEMIS and TES data. (top) Daytime zonally averaged dust (1075 cm^{-1}) and water ice (825 cm^{-1}) optical depth as a function of season (L_s) and latitude, as retrieved from THEMIS data. (bottom) Same as in Figure 6 (top), but as retrieved from TES data. The data from each instrument has been binned (2° in L_s and 10° in latitude) to ease comparison. The color scale goes from 0 (purple) to 0.25 (red).

depth over that period. The local time for the observations varies from roughly 1500 LT in the beginning to 1710 LT at the end. The retrieval of aerosol optical depth is restricted to those spectra with a surface temperature greater than 210 K to ensure adequate thermal contrast between the surface and the atmosphere. Because dust optical depth is usually nearly well mixed with CO_2, it has been scaled to a 6.1 mbar equivalent pressure surface to remove the effect of topography. Water ice optical depth is not well mixed and so is not scaled.

4.1. Dust Optical Depth

[32] Figure 4 (top) shows zonally averaged daytime dust optical depth at 1075 cm^{-1} scaled to an equivalent 6.1 mbar surface as a function of L_s and latitude as retrieved from THEMIS observations. THEMIS began mapping in the decay of a moderate regional dust storm. The dust storm was observed by TES to have begun at $L_s \sim 315°$ [*Smith et al.*, 2003]. Maximum optical depth of between 0.25 and 0.3 was found at low latitudes at $L_s = 330°$. Dust optical depth gradually decreased to less than 0.1 by $L_s = 25°$ and remained low until $\sim L_s = 140°$ when dust activity began to increase, especially south of the equator. Occasional local-scale enhancements in dust optical depth were also observed along the edge of the retreating northern seasonal polar ice cap.

[33] Figure 4 (bottom) shows a latitude-longitude map of dust optical depth between $L_s = 330°$ and $350°$. The most active region of this regional dust storm was in Margaritifer Terra and Xanthe Terra, just west of the prime meridian and near the equator. Previous observations of regional dust storms at this L_s in previous years have occurred in the same

location [*Smith et al.*, 2000a, 2001a]. The coverage of the map is spotty because THEMIS observations are targeted at specific areas of interest rather than taken systematically from pole to pole as with TES.

4.2. Water Ice Optical Depth

[34] Figure 5 (top) shows zonally averaged daytime water ice optical depth at 825 cm^{-1} as a function of L_s and latitude. The initiation and growth of the annual aphelion season cloud belt is very evident. There were few water ice clouds at the beginning of THEMIS mapping, but cloud optical depth steadily increased after $L_s = 0°$ reaching their full latitudinal extent by about $L_s = 60°$. Although cloud optical depth continued to increase after $L_s = 100°$ we will see in the following sections that this was primarily caused by THEMIS observations progressing to later local times.

[35] Figure 5 (bottom) is a latitude-longitude map of water ice cloud optical depth between $L_s = 60°$ and $120°$ while the aphelion season cloud belt was active. The spatial distribution of cloud cover is similar to that observed by TES [*Pearl et al.*, 2001; *Smith et al.*, 2001a, 2001b]. Significant cloud cover existed from roughly 10°S to 30°N latitude with larger optical depth over elevated topography such as Elysium, Tharsis, Olympus Mons, and Alba Patera.

4.3. Comparison With TES Aerosol Optical Depth

[36] The THEMIS and TES instruments observe the same dust and water ice absorption features and so a direct comparison can be made between the aerosol optical depth retrieved from the two instruments. Figure 6 (top) shows dust (1075 cm^{-1}) and water ice (825 cm^{-1}) optical depth as

a function of season (L_s) and latitude as retrieved from THEMIS infrared spectra. Figure 6 (bottom) shows the same quantities as retrieved from TES infrared spectra. The data have been placed in bins 2° wide in L_s and 10° wide in latitude to ease comparison. The seasonal and latitudinal trends for THEMIS and TES are very similar. Both show decay of a regional dust storm early in the period, elevated dust optical depth at high northern latitudes during northern spring, and increased dust activity after $L_s \sim 130°$ in southern low latitudes. Both TES and THEMIS show the aphelion season water ice cloud belt beginning to become prominent at $L_s \sim 30°$ and reaching full latitudinal extent by about $L_s = 60°$. The amplitudes of THEMIS and TES dust and water ice optical depth are within ±20% of each other (consistent with estimated uncertainties) for nearly all times.

[37] Although the trends are mostly similar, there are some differences. The largest differences are in water ice optical depth at high northern and southern latitudes. TES retrievals show increased water ice cloud optical depth at $L_s = 20°-30°$ at the highest southern latitudes and during the period $L_s = 330°-75°$ at the highest northern latitudes that is absent from the THEMIS retrievals. These clouds observed by TES could be associated with polar hoods. Although TES and THEMIS both observe dust in the northern hemisphere at $L_s = 0°-100°$ and at all latitudes after $L_s = 130°$ the optical depth from TES tends to be a little bit higher. It is not immediately obvious why these differences exist. The spatial coverage for THEMIS is not as uniform or as complete as for TES, and it is possible that local and short-lived dust storms could be observed by one instrument but not by the other.

4.4. Diurnal Variation of Dust and Water Ice Clouds

[38] Because Mars Global Surveyor (TES) and Mars Odyssey (THEMIS) are in different orbits at different local times of day, concurrent observations by the THEMIS and TES instruments allow some limited sampling of the diurnal variation of aerosol optical depth. At the beginning of Odyssey mapping ($L_s = 330°$), THEMIS observed a local time of about 1500 LT while TES observed at about 1320 LT (at the equator). The local time observed by both instruments monotonically (and nearly linearly) progressed toward later times throughout the period covered here. By $L_s = 160°$, THEMIS observed a local time of about 1710 LT while TES observed at about 1440 LT (at the equator).

[39] Figure 7 (top) shows the ratio of THEMIS water ice optical depth to TES water ice optical depth as a function of THEMIS local time. The ratio was performed on an average of all retrievals from 30°N to 30°S latitude. Given the estimated uncertainties in both THEMIS and TES retrievals, the estimated uncertainty in this ratio is ±0.2. Figure 7 (bottom) shows the relationship between the local times observed by THEMIS and TES. The ratio of THEMIS to TES dust optical depth (not shown in Figure 7) is between 0.8 and 1.2 during the entire period, which is consistent with THEMIS and TES observing the same optical depth. The ratio of THEMIS to TES water ice optical depth is near unity until about $L_s = 90°$ when THEMIS local time is 1630 LT at which time the ratio rises rapidly to about 1.4 at $L_s = 160°$ when THEMIS local time was 1710 LT. We believe that the ratio of 1.4 indicates a real difference. This
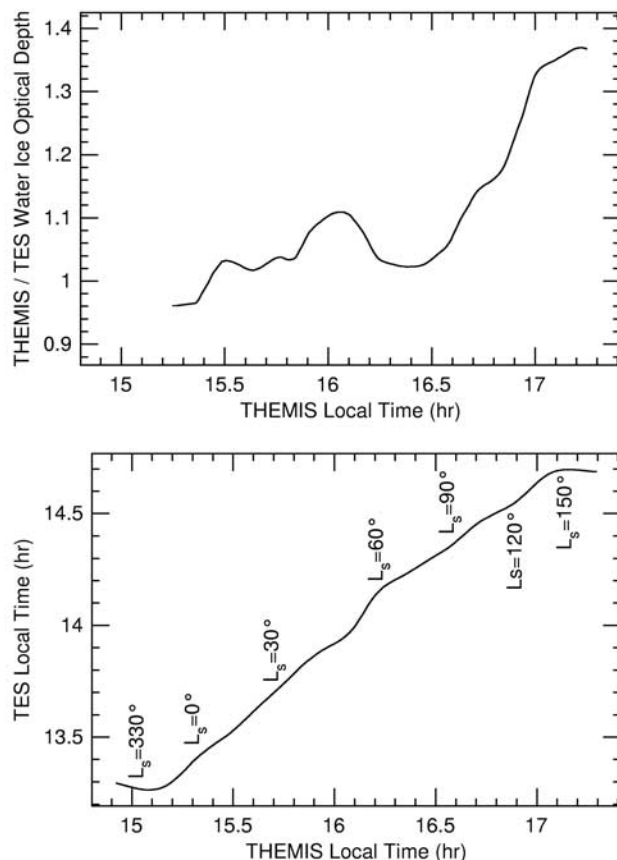

Figure 7. (top) Ratio of water ice aerosol optical depth retrieved using THEMIS to that retrieved from TES data, as a function of THEMIS local time. All data between 30°N and 30°S latitude were included. The estimated uncertainty in this ratio is ±0.2, so values for the ratio between 0.8 and 1.2 are consistent with TES and THEMIS observations showing the same optical depth. Water ice seems to show a local time dependence with increased optical depth in the late afternoon. (bottom) The relationship between THEMIS local time, TES local time, and L_s.

difference between THEMIS and TES is also apparent in Figure 6, where THEMIS water ice optical depth stays nearly constant at low latitudes after $L_s = 120°$ while TES water ice optical depth decreases.

[40] A portion of the difference between THEMIS and TES optical depth may be caused by our assumption that atmospheric temperatures observed by TES can be used as representative of those observed by THEMIS. If atmospheric temperatures are in fact lower for THEMIS (later in the day) than for TES, then the thermal contrast between the surface and atmosphere is actually greater than we assume and less aerosol is required to produce the observed depth of aerosol spectral features. We have performed numerical experiments that show that a decrease in atmospheric temperature at all levels of 5 K results in the water ice ratio falling from 1.4 to about 1.2. Although it is possible that this effect could explain part of the increase in the water ice optical depth ratio after $L_s = 90°$, it does not appear to be large enough to be the sole reason for the increase.

[41] The difference in water ice optical depth between 1700 LT observed by THEMIS and 1430 LT observed by

TES appears to be real. Maps of the spatial distribution of clouds show little difference between THEMIS observations after $L_s = 120°$ (when THEMIS water ice clouds are enhanced relative to TES) and the period $L_s = 60°–120°$ (Figure 5 (bottom); when THEMIS and TES show similar water ice optical depth). The dependence of the water ice optical depth ratio on THEMIS local time (as shown in Figure 7 (top)) indicates that the main enhancement in water ice optical depth occurs after about 1630 LT. THEMIS observations are in general agreement with the diurnal variation in water ice cloud optical depth that has previously been observed a number of times. Observations of water ice clouds from ground-based telescopes [e.g., *Smith and Smith*, 1972; *Akabane et al.*, 2002; *Glenar et al.*, 2003], the Hubble Space Telescope [*Clancy et al.*, 1996; *Wolff et al.*, 1999], the Viking IRTM [*Christensen*, 1998], and the Mars Global Surveyor Mars Orbiter Camera [*Benson et al.*, 2002; B. Cantor and M. Malin, personal communication, 2003] all show minimum water ice cloud optical depth near noon or early afternoon with higher optical depth in both the early morning and late afternoon.

5. Summary

[42] Infrared data from the Thermal Emission Imaging System (THEMIS) are well suited for providing quantitative information about atmospheric dust and water ice aerosol optical depth. Atmospheric observations by THEMIS provide the potential to complement the extensive atmospheric data concurrently being returned by MGS TES by offering observations at a later local time. Furthermore, the small spatial scale that can be resolved by THEMIS potentially allows the study of phenomena not visible from TES such as dust devils.

[43] At the beginning of THEMIS mapping ($L_s = 330°$), dust optical depth was relatively high ($0.2–0.3$) as THEMIS observed the decay of a regional dust storm centered in Margaritifer Terra and Xanthe Terra. Water ice optical depth was very low (<0.05). Dust settled out and low-latitude optical depth dropped below 0.1 by $L_s = 25°$. The annual minimum in global dust loading was observed between $L_s = 60°$ and $130°$. During northern spring ($L_s = 0°–90°$), THEMIS observed moderate dust activity along the edge of the retreating north polar seasonal cap. Also during that time the low-latitude aphelion season water ice cloud belt formed. The cloud belt reached full latitudinal extent (10°S to 30°N latitude) by $L_s = 60°$, but continued to increase in optical depth until at least $L_s = 120°$. The polar hoods in both the northern and southern hemispheres were far less pronounced in THEMIS data than in TES data.

[44] As the season progressed, the orbit of the Odyssey spacecraft moved to increasingly later local time. By $L_s = 160°$, the local time at the equator was 1710 LT. Water ice optical depth retrieved from THEMIS after $L_s = 120°$ (at ~1700 LT) was significantly higher than that retrieved from TES (at 1430–1445 LT), suggesting a diurnal variation in cloud optical depth. Concurrent observations by TES and THEMIS are continuing. Throughout the remainder of the nominal Odyssey mission, the local solar time for THEMIS observations will be between 1600 and 1730 LT. The local time difference of nearly 3 hours between THEMIS and TES observations will allow some measure of the diurnal variation of aerosols (especially water ice clouds) to be determined.

References

Akabane, A., T. Nakakushi, K. Iwasaki, and S. M. Larson, Diurnal variation of Martian water-ice clouds in Tharsis region of the low latitude cloud belt: Observations in 1995–1999 apparitions, *Astron. Astrophys.*, *384*, 678–688, 2002.

Bandfield, J. L., and M. D. Smith, Multiple emission angle surface-atmosphere separations of Thermal Emission Spectrometer data, *Icarus*, *161*, 47–65, 2003.

Bandfield, J. L., P. R. Christensen, and M. D. Smith, Spectral data set factor analysis and end-member recovery: Application to analysis of Martian atmospheric particulates, *J. Geophys. Res.*, *105*, 9573–9588, 2000a.

Bandfield, J. L., V. E. Hamilton, and P. R. Christensen, A global view of Martian surface composition from MGS-TES, *Science*, *287*, 1626–1630, 2000b.

Benson, J. L., B. P. Bonev, P. B. James, K. J. Shan, B. A. Cantor, and M. A. Caplinger, A study of seasonal and short period variation of water ice clouds in the Tharsis and Valles Marineris regions of Mars with Mars Global Surveyor (abstract), *Bull. Am. Astron. Soc.*, *34*, 863, 2002.

Chase, S. C., Jr., J. L. Engel, H. W. Eyerly, H. H. Kieffer, F. D. Palluconi, and D. Schofield, Viking infrared thermal mapper, *Appl. Opt.*, *17*, 1243–1251, 1978.

Christensen, P. R., Variations in Martian surface composition and cloud occurrence determined from thermal infrared spectroscopy: Analysis of Viking and Mariner 9 data, *J. Geophys. Res.*, *103*, 1733–1746, 1998.

Christensen, P. R., et al., Thermal emission spectrometer experiment: Mars Observer mission, *J. Geophys. Res.*, *97*, 7719–7734, 1992.

Christensen, P. R., et al., Detection of crystalline hematite mineralization on Mars by the Thermal Emission Spectrometer: Evidence for near-surface water, *J. Geophys. Res.*, *105*, 9632–9642, 2000.

Christensen, P. R., et al., Mars Global Surveyor Thermal Emission Spectrometer experiment: Investigation description and surface science results, *J. Geophys. Res.*, *106*, 23,823–23,871, 2001.

Christensen, P. R., et al., The Thermal Emission Imaging System (THEMIS) for the Mars 2001 Odyssey mission, *Space Sci. Rev.*, in press, 2003a.

Christensen, P. R., et al., Morphology and composition of the surface of Mars: Mars Odyssey THEMIS results, *Science*, *300*, 2056–2061, 2003b.

Clancy, R. T., A. W. Grossman, M. J. Wolff, P. B. James, D. J. Rudy, Y. N. Billawala, B. J. Sandor, S. W. Lee, and D. O. Muhleman, Water vapor saturation at low altitudes around Mars aphelion: A key to Mars climate?, *Icarus*, *122*, 36–62, 1996.

Clancy, R. T., B. J. Sandor, M. J. Wolff, P. R. Christensen, M. D. Smith, J. C. Pearl, B. J. Conrath, and R. J. Wilson, An intercomparison of ground-based millimeter, MGS TES, and Viking atmospheric temperature measurements: Seasonal and interannual variability of temperatures and dust loading in the global Mars atmosphere, *J. Geophys. Res.*, *105*, 9553–9572, 2000.

Clancy, R. T., M. J. Wolff, and P. R. Christensen, Mars aerosol studies with the MGS TES emission phase function observations: Optical depths, particle sizes, and ice cloud types versus latitude and solar longitude, *J. Geophys. Res.*, *108*(E9), 5098, doi:10.1029/2003JE002058, 2003.

Conrath, B. J., J. C. Pearl, M. D. Smith, W. C. Maguire, P. R. Christensen, S. Dason, and M. S. Kaelberer, Mars Global Surveyor Thermal Emission Spectrometer (TES) observations: Atmospheric temperatures during aerobraking and science phasing, *J. Geophys. Res.*, *105*, 9509–9520, 2000.

Glenar, D. A., R. E. Samuelson, J. C. Pearl, G. L. Bjoraker, and D. Blaney, Spectral imaging of Martian water ice clouds and their diurnal behavior during the 1999 aphelion season, *Icarus*, *161*, 297–318, 2003.

Hanel, R., et al., Investigation of the Martian environment by infrared spectroscopy on Mariner 9, *Icarus*, *17*, 423–442, 1972.

Jaquin, F., P. J. Gierasch, and R. Kahn, The vertical structure of limb hazes in the Martian atmosphere, *Icarus*, *68*, 442–461, 1986.

Kieffer, H. H., T. Z. Martin, A. R. Peterfreund, B. M. Jakosky, E. D. Miner, and F. D. Palluconi, Thermal and albedo mapping of Mars during the Viking primary mission, *J. Geophys. Res.*, *82*, 4249–4292, 1977.

Liu, J., M. I. Richardson, and R. J. Wilson, An assessment of the global, seasonal, and interannual spacecraft record of Martian climate in the thermal infrared, *J. Geophys. Res.*, *108*(E8), 5089, doi:10.1029/2002JE001921, 2003.

Martin, T. Z., and H. H. Kieffer, Thermal infrared properties of the Martian atmosphere: 2. The 15-μm band measurements, *J. Geophys. Res.*, *84*, 2843–2852, 1979.

Pearl, J. C., M. D. Smith, B. J. Conrath, J. L. Bandfield, and P. R. Christensen, Observations of Martian ice clouds by the Mars Global Surveyor Thermal Emission Spectrometer: The first Martian year, *J. Geophys. Res.*, *106*, 12,325–12,338, 2001.

Pollack, J. B., D. Colburn, R. Kahn, J. Hunter, W. Van Camp, C. E. Carlston, and M. R. Wolf, Properties of aerosols in the Martian atmosphere, as inferred from Viking lander imaging data, *J. Geophys. Res.*, *82*, 4479–4496, 1977.

Smith, S. A., and B. A. Smith, Diurnal and seasonal behavior of discrete white clouds on Mars, *Icarus*, *16*, 509–521, 1972.

Smith, P. H., et al., Results from the Mars Pathfinder Camera, *Science*, *278*, 1758–1765, 1997.

Smith, M. D., J. C. Pearl, B. J. Conrath, and P. R. Christensen, Mars Global Surveyor Thermal Emission Spectrometer (TES) observations of dust opacity during aerobraking and science phasing, *J. Geophys. Res.*, *105*, 9539–9552, 2000a.

Smith, M. D., J. L. Bandfield, and P. R. Christensen, Separation of atmospheric and surface spectral features in Mars Global Surveyor Thermal Emission Spectrometer (TES) spectra, *J. Geophys. Res.*, *105*, 9589–9608, 2000b.

Smith, M. D., J. C. Pearl, B. J. Conrath, and P. R. Christensen, Thermal Emission Spectrometer results: Mars atmospheric thermal structure and aerosol distribution, *J. Geophys. Res.*, *106*, 23,929–23,945, 2001a.

Smith, M. D., J. C. Pearl, B. J. Conrath, and P. R. Christensen, One Martian year of atmospheric observations by the Thermal Emission Spectrometer, *Geophys. Res. Lett.*, *28*, 4263–4266, 2001b.

Smith, M. D., B. J. Conrath, J. C. Pearl, and P. R. Christensen, TES observations of aerosol optical depth and water vapor abundance, paper presented at the International Workshop: Mars Atmosphere Modeling and Observations, Atmos. Infrared Emiss. Group, Granada, Spain, 13–15 Jan. 2003.

Wilson, R. J., and M. I. Richardson, The Martian atmosphere during the Viking mission, I: Infrared measurements of atmospheric temperatures revisited, *Icarus*, *145*, 555–579, 2000.

Wolff, M. J., and R. T. Clancy, Constraints on the size of Martian aerosols from Thermal Emission Spectrometer observations, *J. Geophys. Res.*, *108*(E9), 5097, doi:10.1029/2003JE002057, 2003.

Wolff, M. J., J. F. Bell III, P. B. James, R. T. Clancy, and S. W. Lee, Hubble Space Telescope observations of the Martian aphelion cloud belt prior to the Pathfinder mission: Seasonal and interannual variations, *J. Geophys. Res.*, *104*, 9027–9041, 1999.

————————————

J. L. Bandfield and P. R. Christensen, Department of Geology, Arizona State University, P.O. Box 871404, Tempe, AZ 85287, USA. (joshband@imap3.asu.edu; phil.christensen@asu.edu)

M. I. Richardson, Division of Geological and Planetary Sciences, California Institute of Technology, MS 150-21, Pasadena, CA 91125, USA. (mir@gps.caltech.edu)

M. D. Smith, NASA Goddard Space Flight Center, Mail Code 693, Greenbelt, MD 20771, USA. (michael.d.smith@nasa.gov)